GDCh Research Article Angewandte International Edition Chemie www.angewandte.org

How to cite: *Angew. Chem. Int. Ed.* **2026**, *65*, e19793
doi.org/10.1002/anie.202519793

Redox Flow Batteries **Hot Paper**

Structurally Asymmetric Nonplanar π-Conjugated Naphthoquinone Derivatives Modified from Natural Lawsone for High-Stability Aqueous Redox Flow Batteries

*Pengbo Zhang[+], Sheng Wen[+], Yongkang Chen[+], Yuzhu Liu, Jie Wei, Zuoao Wu, Guochun Ding, Xinmei Song, Tengfei Dai, Zhihu You, Qingbo Guo, Peng Liu, Jianwen Guo, Zuoxiu Tie, and Zhong Jin**

Abstract: Aqueous organic redox flow batteries (AORFBs) have attracted growing interest for grid-scale energy storage by reducing reliance on scarce mineral resources used in transition metal-based systems. Natural naphthoquinone derivatives, while environmentally friendly and abundant, suffer from poor solubility and electrochemical instability, hindering their practical use in AORFBs. To address these challenges, we report the functionalization of a naturally abundant dye, lawsone (i.e., 2-HNQ), through non-planar π-conjugation extension and asymmetric intramolecular charge distribution, yielding a non-planar π-conjugated polar naphthoquinone derivative (namely BANQ) with enhanced water solubility and redox reversibility. Computational simulations and spectroscopic analysis confirmed that the introduction of benzoic acid group imparts a polar π-conjugation extended structure with asymmetric charge distribution. This structural modification efficiently enhances aqueous solubility and suppresses degradation pathways, such as Michael addition and irreversible keto-enol tautomerism. Compared with 2-HNQ precursor, BANQ exhibits lower sensitivity to nucleophilic and electrophilic attacks. The BANQ anolyte exhibited a very low-capacity decay rate of merely 0.00018% per cycle (or 0.045% per day), representing a two-order-of-magnitude reduction compared to that of 2-HNQ (0.032% per cycle or 8.22% per day). This study highlights the potential of modifying natural-derived products with rationally designed conjugated electron structure for green and sustainable energy storage solutions.

Introduction

The development of large-scale, cost-effective, and long-duration energy storage systems is of paramount importance in addressing the imbalance between electricity supply and demand, thereby mitigating renewable energy intermittency and ensuring the stable and reliable operation of the power grid.[1–6] Among the various currently available large-scale energy storage technologies, aqueous organic redox flow batteries (AORFBs) have emerged as promising candidates due to their abundant raw material sources, tunable electrochemical properties, and environmental compatibility.[7–9] The intrinsic decoupled design of the liquid redox-active electrolyte from the cell stack enables flexible adjustment of storage capacity and power output by modulating the electrolyte volume, thereby accommodating diverse energy demands and grid specifications.[10–12]

In recent years, quinone compounds, especially side-chain functionalized anthraquinone derivatives, have garnered increasing attention as redox-active materials used for alkaline AORFBs.[13–15] In contrast, naphthoquinone derivatives, despite their higher natural abundance, are rarely deployed in AORFBs owing to their low electrochemical stability compared to those of anthraquinones.[16] For example, a natural dye, lawsone (2-hydroxy-1,4-naphthoquinone, i.e., 2-HNQ), can be abundantly extracted from the leaves of henna plants and the flowers of water hyacinths, offering environmental friendliness and low-cost scalability. However, the limited water solubility and poor electrochemical stability of pristine 2-HNQ hinder its use in AORFBs.[16–21] The C─H bond adjacent to the C═O group in 2-HNQ is prone to the Michael addition reaction in alkaline media, leading to degradation by nucleophiles during cycling. Additionally, the enol-keto tautomerism of reduced 2-HNQ is thermodynamically favorable, resulting in its degradation to 2,3-dihydrobislawsone and, consequently, causing severe capacity decay of AORFBs.[22,23] Thus, the enhancement of aqueous solubility and cycling stability of natural naphthoquinone derivatives through rational molecular design remains a pivotal challenge to be addressed.

[*] P. Zhang[+], S. Wen[+], Y. Chen[+], Y. Liu, J. Wei, Z. Wu, G. Ding, X. Song, T. Dai, Z. You, Q. Guo, P. Liu, J. Guo, Z. Tie, Z. Jin
State Key Laboratory of Coordination Chemistry, MOE Key Laboratory of Mesoscopic Chemistry, MOE Key Laboratory of High Performance Polymer Materials and Technology, Jiangsu Key Laboratory of Green Energy Catalysis and Intelligent Chemical Engineering, Suzhou Key Laboratory of Green Intelligent Manufacturing of New Energy Materials and Devices, Tianchang New Materials and Energy Technologies Research Center, Institute of Green Chemistry and Engineering, School of Chemistry and Chemical Engineering, Nanjing University, Nanjing, Jiangsu 210023, China
E-mail: zhongjin@nju.edu.cn

[+] These authors contributed equally to this work.

Additional supporting information can be found online in the Supporting Information section

Herein, we propose a non-planar π-conjugation extension strategy to graft a polar benzoic acid side-group onto the 2-HNQ redox core, aiming to enhance both its π-conjugation effect and molecular polarity. Through artificial modification of the natural product 2-HNQ, we successfully synthesized an asymmetric non-planar naphthoquinone derivative 4-(3-hydroxy-1,4-dioxo-1,4-dihydronaphthalen-2-yl)benzoic acid (namely BANQ), which exhibited much higher aqueous solubility and redox reversibility. Theoretical calculations revealed that a specific angle exists between the redox core and the π-conjugated benzoic acid side-group within the BANQ molecule, indicating a unique non-planar configuration. This distinctive geometry, coupled with the strong deprotonation of BANQ under basic conditions, results in a non-equilibrium charge distribution and increased molecular polarization, thereby highly enhancing its solubility in water under alkaline conditions. Distinct from 2-HNQ that is thermodynamically unstable and susceptible to enol-keto tautomerization during cycling, BANQ exhibits good thermodynamic stability and preserves the intact integrity of its redox core structure. The condensed Fukui function (CFF) calculations indicated that the redox core of BANQ, characterized by its asymmetric non-planar π-conjugation structure, is much better protected and less susceptible to nucleophilic/electrophilic attacks compared to 2-HNQ, resulting in enhanced cycling stability. The capacity decay rate of BANQ anolyte was observed to be only 0.00018% per cycle (or 0.045% per day). In contrast, the natural 2-HNQ anolyte exhibited a capacity decay rate of 0.032% per cycle (or 8.22% per day), representing a stability inferiority of two orders of magnitude. These findings demonstrate that asymmetric non-planar π-conjugation extension highly enhances the electrochemical performance of naphthoquinone derivatives, paving the way for developing artificially modified natural products to create fascinating organic redox-active compounds toward large-scale, green and sustainable energy storage applications.

Results and Discussion

The asymmetric non-planar π-conjugated BANQ molecule was synthesized through a Suzuki-Miyaura coupling reaction, as depicted in Figure 1a.[24,25] The product obtained from each synthetic step was verified via ^{1}H and ^{13}C nuclear magnetic resonance (NMR) spectra, and the final BANQ molecule was further confirmed in terms of molecular structure and purity by high-resolution mass spectrometry (HRMS) and elemental analysis (Figures S1–S5). Besides this palladium-catalyzed reaction route, a cost-effective and scalable Pd-free diazotization-substitution pathway was also developed (Scheme S1), providing an alternative synthesis route that avoids the use of expensive Pd catalysts.[26,27] The aqueous solubilities of 2-HNQ and BANQ were assessed under alkaline conditions (pH 14) by utilizing ultraviolet-visible (UV–vis) absorption spectroscopy (Figures S6 and S7). The solubility of BANQ was determined to be 1.3 M, far surpassing that of 2-HNQ (merely 0.04 M). The enhanced solubility is ascribed to the asymmetric non-planar conjugation and rotatable structure of BANQ (with a favored conformation of 52.85°, Figure S8) and its strong deprotonation under alkaline conditions, leading to a non-equilibrium charge distribution and increased molecular polarization and thus strongly enhancing its solubility in water under alkaline conditions. This finding underscores the pivotal role of non-planar and charge asymmetry design in optimizing the physicochemical properties of redox-active molecules. The viscosities of BANQ anloytes with various concentrations in 1.0 M KOH solutions are depicted in Figure S9. Even at high concentrations, the BANQ anolytes still exhibited low viscosities (1.32 mPa·s for 0.5 M BANQ and 2.43 mPa·s for 1.0 M BANQ), suggesting its high flowability and practical applicability.

It has been reported that the C─H site adjacent to the C═O functional group in the 2-HNQ molecule is highly reactive.[28,29] To better understand this reactivity at the molecular orbital level, we employed Kenichi Fukui's frontier orbital theory to predict the active sites of electrophilic or nucleophilic reactions based on the contributions of the highest occupied molecular orbital (HOMO) and lowest unoccupied molecular orbital (LUMO).[30] This prediction involves examining the total electron density ($\rho_i = |\varphi_i|^2$) of a given orbital (i) around each atom. Consequently, sites with larger Fukui function values exhibit higher reactivity. Furthermore, we calculated and visualized the condensed Fukui function (CFF) for electrophilic/nucleophilic reactions using Gaussian 16 software at the density functional theory (DFT) B3LYP/6-311+G(d, p) level, combined with the MultiWFN 3.8 program, following the detailed protocols described in previous literature.[31,32] The CFF calculations revealed that the asymmetric π-conjugated extension structure of BANQ substantially diminishes the reactivity of active C─H sites toward electrophilic reactions compared to the natural 2-HNQ precursor. Given the elevated concentration of nucleophiles in alkaline conditions, this finding supports the enhanced stability of BANQ under such conditions.[16,17] Additionally, in its reduced state, reduced BANQ (*re*-BANQ) exhibits a decreased propensity for nucleophilic reactions compared to reduced 2-HNQ (*re*-2-HNQ), highlighting the crucial role of the benzoic acid moiety in enhancing the stability of its reduced state (Figure 1b).

The electrochemical properties of 2-HNQ and BANQ in 1.0 M KOH solution were evaluated using cyclic voltammetry (CV), as shown in Figure 1c. For BANQ, a redox peak appeared at –0.74 V (vs. Ag/AgCl), with a peak separation (ΔE) of 56.9 mV, corresponding to a two-electron transfer process. In contrast, the reversible potential of 2-HNQ was 30 mV higher than that of BANQ, with a peak separation (ΔE) of 77.4 mV for a two-electron transfer process. This difference was attributed to the electron-donating ability of the π-conjugated benzoic acid group, and the extended π-conjugation structure of BANQ further contributes to its enhanced redox reversibility.[33] Figure 1d illustrates the structural configuration and charge/discharge processes of the BANQ||$K_4Fe(CN)_6$ AORFBs, which utilize a customized, low-cost sulfonated polyetheretherketone (SPEEK) membrane. When the BANQ anolyte is paired with the potassium ferrocyanide catholyte, the theoretical equilibrium cell voltage is 1.02 V.

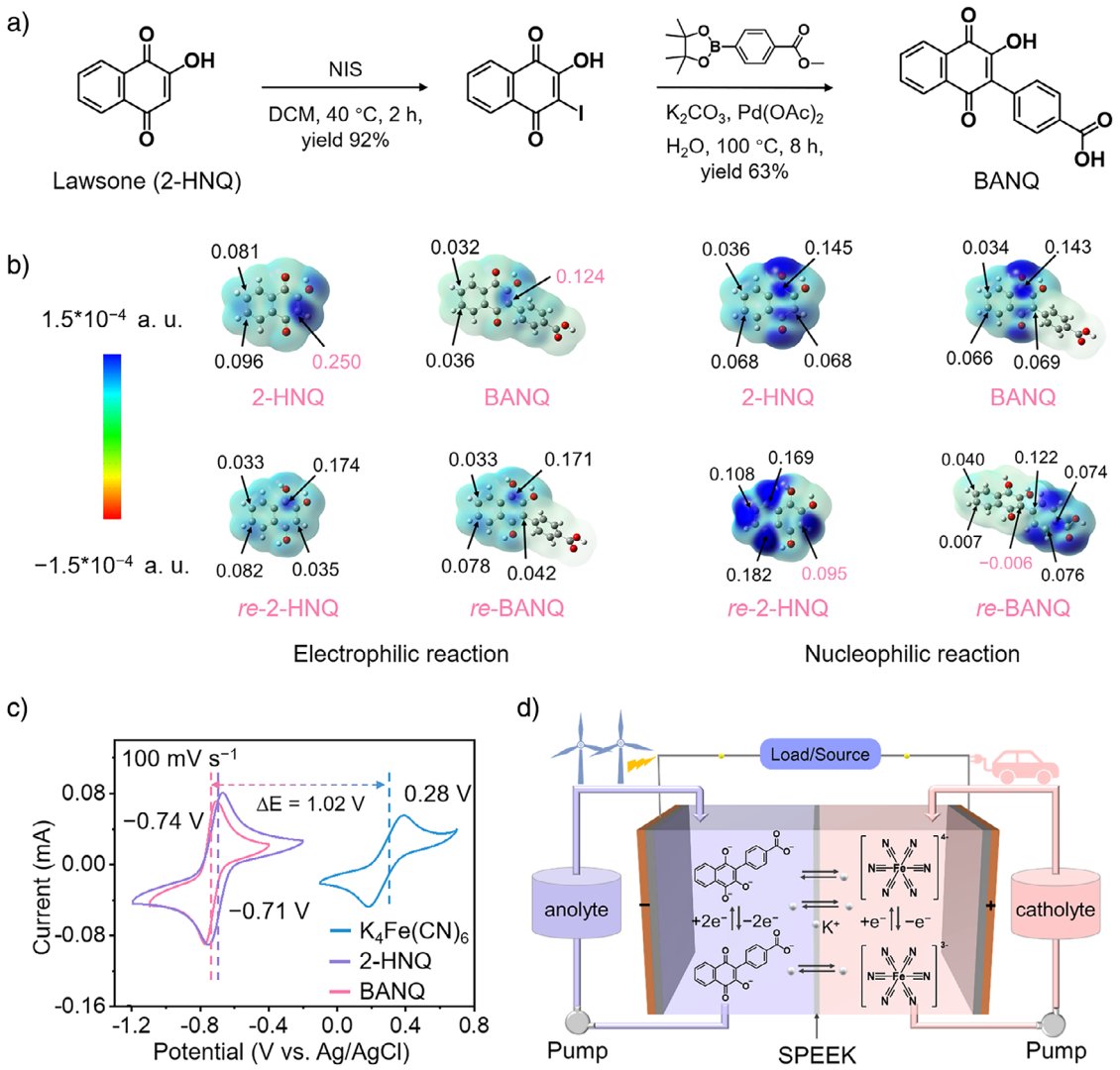

Figure 1. Synthesis route, theoretical calculations and properties of BANQ. a) The synthesis process of BANQ. b) CFF calculations of 2-HNQ and BANQ molecules performed using Gaussian 16 and the MultiWFN 3.8 programs at the DFT B3LYP/6-311+G(d, p) level. c) CV curves of 5 mM 2-HNQ, BANQ and $K_4Fe(CN)_6$ dissolved in 1.0 M KOH solutions at a scan rate of 100 mV s^{-1}. d) Structural configuration of the AORFBs based on BANQ anolyte paired with ferrocyanide catholyte.

The pH-dependent structural transitions of 2-HNQ and BANQ were systematically investigated by UV–vis absorption spectroscopy.[34] As shown in Figure 2a and Figure S10, the phenolic hydroxyl group in 2-HNQ exhibits a p*Ka* of 4, as determined from its UV–vis absorption spectra at λ_{453} nm under different pH conditions. The asymmetric non-planar π-conjugated BANQ, characterized by the presence of both phenolic hydroxyl and carboxyl groups, exhibits more complex dissociation equilibria. This is further supported by the analysis of the absorbance at λ_{462} nm (Figure 2b and Figure S11), which reveals two distinct p*Ka* values: 1.3 for the carboxyl group and 4.2 for the phenolic hydroxyl group. Furthermore, time-dependent density functional theory (TDDFT) calculations were performed to simulate the UV–vis absorption spectra of the two molecules and to evaluate the contributions of individual excited states.[35] Notably, the simulated UV–vis absorption spectra closely align with the corresponding experimental measurements (Figure 2c and Figure 2d). Compared to 2-HNQ, BANQ exhibits a slight red shift in its UV–vis absorption spectrum, accompanied by less pronounced shoulder peaks. These differences in the UV–vis absorption profiles between BANQ and 2-HNQ are attributed to the introduction of the π-conjugated benzoic acid group, which effectively modulates the internal charge distribution within the molecular framework. Further analysis reveals that in the case of 2-HNQ, the absorption peaks above 300 nm are influenced by the S0→S4 excitation, while those below 300 nm are affected by S0→S5, S7, S8, and S10 excitations. In contrast, the partially twisted π-conjugation structure of BANQ renders it more responsive to UV–vis excitation, involving a higher number of accessible excited states. To elucidate the influence of the benzoic acid group on π-conjugation, the HOMO and LUMO energy levels of 2-HNQ and BANQ in their oxidized/reduced states were

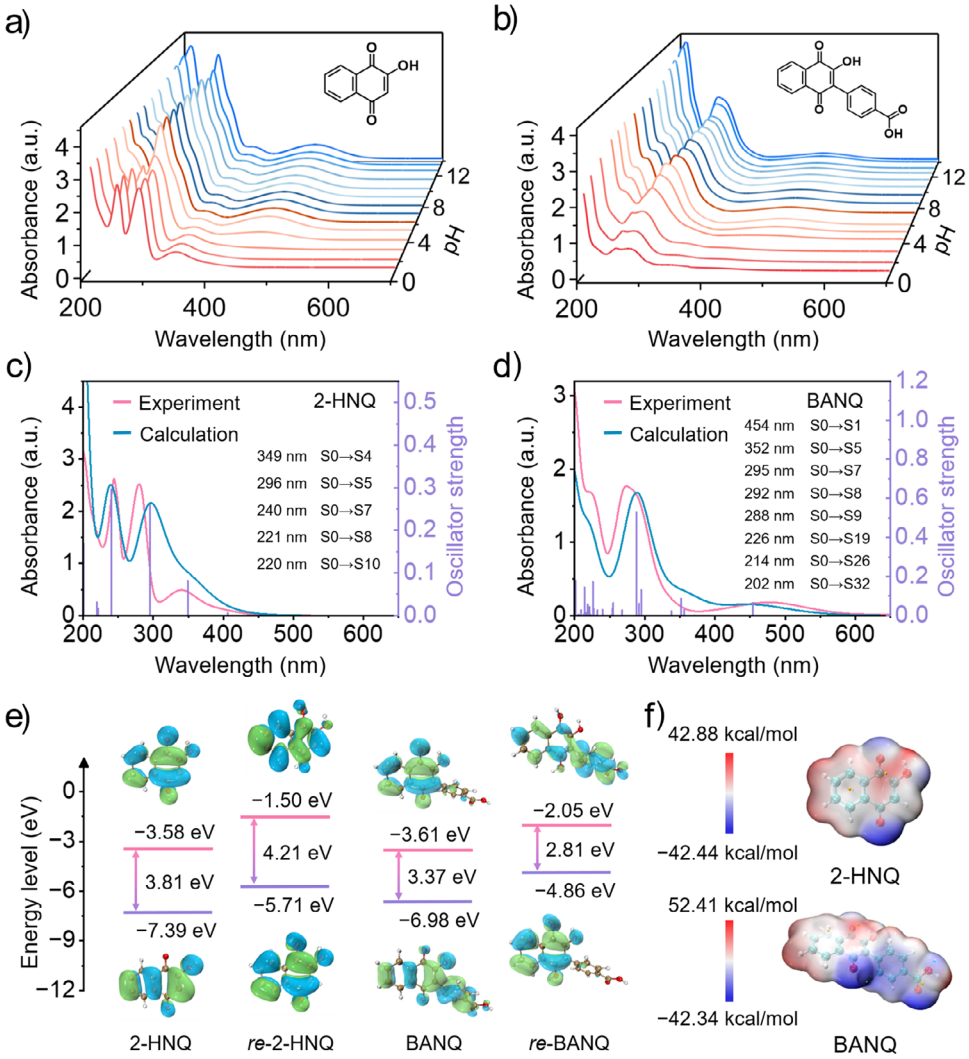

Figure 2. Physicochemical property comparisons of 2-HNQ and BANQ. a, b) UV–vis absorption spectra of (a) 2-HNQ and (b) BANQ solutions at different pH values. c, d) Simulated UV–vis absorption spectra of (c) 2-HNQ and (d) BANQ calculated by the TDDFT method. e) Calculated molecular orbitals and energy gaps of 2-HNQ and BANQ at oxidized (initial) state and reduced state. f) Optimized structures and electrostatic potentials of 2-HNQ and BANQ.

compared through DFT calculations (Figure 2e).[36,37] The LUMO energy level of BANQ (−3.61 eV) closely resembles that of 2-HNQ (−3.58 eV), indicating similar reduction tendencies. However, the HOMO energy level of *re*-BANQ (−4.86 eV) is much higher than that of *re*-2-HNQ (−5.71 eV), suggesting that BANQ exhibits a higher propensity for oxidation. These findings from DFT calculations align well with the trends observed in the CV curves of 2-HNQ and BANQ (Figure 1c). Specifically, the HOMO-LUMO level difference (ΔE) for 2-HNQ and *re*-2-HNQ are 3.81 eV and 4.21 eV, while those for BANQ and *re*-BANQ are 3.37 eV and 2.81 eV, respectively. This indicates that BANQ possesses lower redox barriers, attributable to the π-conjugation effect introduced by the benzoic acid group. DFT simulations were further conducted to study the optimized structures and electrostatic potentials (ESPs) of 2-HNQ and BANQ.[38] As depicted in Figure 2f, the incorporation of the benzoic acid unit in BANQ results in a more negative ESP compared to that of 2-HNQ. The presence of the deprotonated carboxyl group, together with the torsional dihedral angle between the redox core and the benzoic acid side group that allows a certain degree of rotational flexibility, gives rise to an asymmetric charge distribution and enhanced molecular polarizability. These features promote stronger interactions with water molecules, thereby contributing to the improved aqueous solubility of BANQ.

To gain further insights into the proton and electron transfer dynamics during the redox processes following π-conjugated benzoic acid modification, we performed CV analysis of BANQ at varying pH values and constructed a corresponding Pourbaix diagram (Figure S12). The Pourbaix diagram of BANQ presents a slope of 32.5 mV pH^{-1} in the pH range of 10.2–14, corresponding to a single proton/two-electron transfer process. To further investigate the protonation process of BANQ molecules during reduction, we conducted computational studies to quantify the

deprotonation tendencies of carbonyl groups in fully reduced *re*-BANQ molecule (Figure S13). The results show that the two phenolic hydroxyl groups in *re*-BANQ modulate the thermodynamics of carbonyl deprotonation through intramolecular hydrogen bonding. However, these interactions do not alter the overall thermodynamic preference for complete carbonyl deprotonation in *re*-BANQ molecule. To compare the electrochemical kinetics of 2-HNQ and BANQ, their diffusion coefficients (D) were determined by rotating disk electrode (RDE) measurements, while the kinetic rate constants (k_0) were determined and cross-compared based on both RDE analyses and the Nicholson's method.[39] Linear sweep voltammogram (LSV) curves of 5 mM 2-HNQ and BANQ in 1 M KOH solution were recorded with a glassy carbon electrode at different rotation rates between 200 and 2500 rpm (Figures S14–S16). Using the Levich equation, the diffusion coefficients of 2-HNQ and BANQ were calculated to be 5.20×10^{-6} and 2.85×10^{-6} cm^2 s^{-1}, respectively, comparable to those of previously reported naphthoquinone derivatives.[16,17,22] The lower diffusion coefficient of BANQ compared to 2-HNQ is primarily attributed to its larger molecular size. Correspondingly, the k_0 values of 2-HNQ and BANQ determined by RDE analyses were 6.56×10^{-3} and 3.67×10^{-3} cm s^{-1}, respectively. In comparison, by using the Nicholson's method, the k_0 values of 2-HNQ and BANQ were measured to be 2.43×10^{-2} and 3.48×10^{-2} cm s^{-1}, respectively. The discrepancy observed between the two methodologies stems from the fact that Nicholson's method is contingent upon precise peak-to-peak separation and the interpolation of Ψ, factors that can potentially introduce additional sources of error. Overall, its electrochemical performance is impressive and comparable to that of the state-of-the-art naphthoquinone derivatives.[16,17,22]

The electrochemical performances of 0.1 M 2-HNQ and BANQ AORFBs were systematically measured and compared (Figure 3a). The AORFBs were constructed using a custom made SPEEK membrane, thereby reducing the overall cost of the battery system. Electrochemical impedance spectroscopy (EIS) analysis revealed that the resistance value of the SPEEK membrane was 0.39 Ω cm^2 (Figure S17). Typically, 0.1 M 2-HNQ or BANQ solution was used as the anolyte and an excess amount of $K_4Fe(CN)_6$ solution was used as the catholyte, respectively. First, the peak power densities of 0.1 M 2-HNQ||$K_4Fe(CN)_6$ and BANQ||$K_4Fe(CN)_6$ AORFBs were measured at different states of charges (SOCs), including 20%, 50%, and 100%. At 100% SOC, the peak power densities for the 2-HNQ and BANQ based prototype devices were determined as 108 and 122 mW cm^{-2}, respectively (Figure 3b,c). These values are comparable to those reported for previously studied naphthoquinone derivatives.[16,17,22] Subsequently, we evaluated the rate performance of the 0.1 M 2-HNQ||$K_4Fe(CN)_6$ and BANQ||$K_4Fe(CN)_6$ AORFBs across different current densities (Figure 3d,e). The results indicated that both systems exhibited similar rate capability and charge-discharge characteristics. The discharge capacities of 0.1 M 2-HNQ||$K_4Fe(CN)_6$ AORFBs at 20 and 150 mA cm^{-2} were 4.53 and 3.89 Ah L^{-1} respectively. These values correspond to theoretical capacity utilizations of 84.5% and 72.6%, respectively, indicating a slight decline in capacity utilization with increasing current density. For the 0.1 M BANQ||$K_4Fe(CN)_6$ AORFBs, the discharge capacities at 20 and 150 mA cm^{-2} were 4.76 and 3.95 Ah L^{-1}, corresponding to theoretical capacity utilizations of 88.8% and 73.7%, respectively. The capacity utilization values indicate that 2-HNQ and BANQ both undergo a comprehensive two-electron reaction. Upon analyzing the Coulombic efficiency, energy efficiency, and capacity utilization of both AORFBs as a function of current density (Figure 3f and Figure S15), we observed a linear decrease in energy efficiency and capacity utilization along with the increase in current density. This trend suggests that the electrolytes and SPEEK membrane maintain stable voltammetric characteristics across varying current densities.

Subsequently, long-term cycling tests were performed on 0.1 M 2-HNQ||$K_4Fe(CN)_6$ and BANQ||$K_4Fe(CN)_6$ AORFBs at a current density of 100 mA cm^{-2} (Figure 3g). For the 0.1 M 2-HNQ||$K_4Fe(CN)_6$ AORFBs, an initial discharge capacity of 4.21 Ah L^{-1} was recorded. After 600 cycles (or 2.37 days), the capacity decreased to 3.39 Ah L^{-1}, corresponding to a capacity retention rate of 80.5%. The calculated capacity decay rate for the 0.1 M 2-HNQ||$K_4Fe(CN)_6$ AORFBs was 0.032% per cycle or 8.22% per day. Notably, the Coulombic efficiency remained close to 100%, with an average energy efficiency of 82% (Figure S18). In stark contrast, the 0.1 M BANQ||$K_4Fe(CN)_6$ AORFBs delivered an initial discharge capacity of 4.54 Ah L^{-1}, which was almost fully retained at 4.53 Ah L^{-1} after 1550 cycles (5.83 days), corresponding to a capacity retention rate exceeding 99.98% (Figure 3h). The capacity decay rate for 0.1 M BANQ||$K_4Fe(CN)_6$ AORFBs was only 0.00018% per cycle or 0.045% per day, far outperforming the 0.1 M 2-HNQ||$K_4Fe(CN)_6$ AORFBs. Besides, the Coulombic efficiency remained nearly 100%, with an average energy efficiency of 79%.

To evaluate the molecular stability of 2-HNQ and BANQ at approximately 100% SOC, galvanostatic-potentiostatic cycling tests were performed. Following each galvanostatic cycle, the voltage was held at the set limits (1.5 V during charging, and 0.5 V during discharging) until the current density decreased to 6 mA cm^{-2}, ensuring that all 2-HNQ and BANQ molecules reached their fully reduced states (Figure 3i,j and Figure S19). The results revealed a decrease in the capacity of 0.1 M 2-HNQ||$K_4Fe(CN)_6$ AORFBs from 4.48 Ah L^{-1} to 3.17 Ah L^{-1} after 600 cycles, corresponding to a decay rate of 0.049% per cycle (11.83% per day). The capacity decay rate in the galvanostatic-potentiostatic test exceeded that in the galvanostatic test, suggesting that the cycling stability of 2-HNQ is strongly influenced by the SOCs of the AORFBs. In contrast, the 0.1 M BANQ||$K_4Fe(CN)_6$ AORFBs exhibited much superior stability under galvanostatic-potentiostatic cycling conditions. After 1250 cycles (5.63 days), the discharge capacity declined from 4.77 Ah L^{-1} to 4.73 Ah L^{-1}, corresponding to a minimal capacity decay rate of only 0.00067% per cycle or 0.15% per day. This finding underscores the favourable electrochemical stability of the 0.1 M BANQ||$K_4Fe(CN)_6$ AORFBs at 100% SOC. The cycling stability of BANQbased AORFBs demonstrates an improvement of nearly two orders of magnitude compared to that of 2-HNQ, highlighting the crucial role of

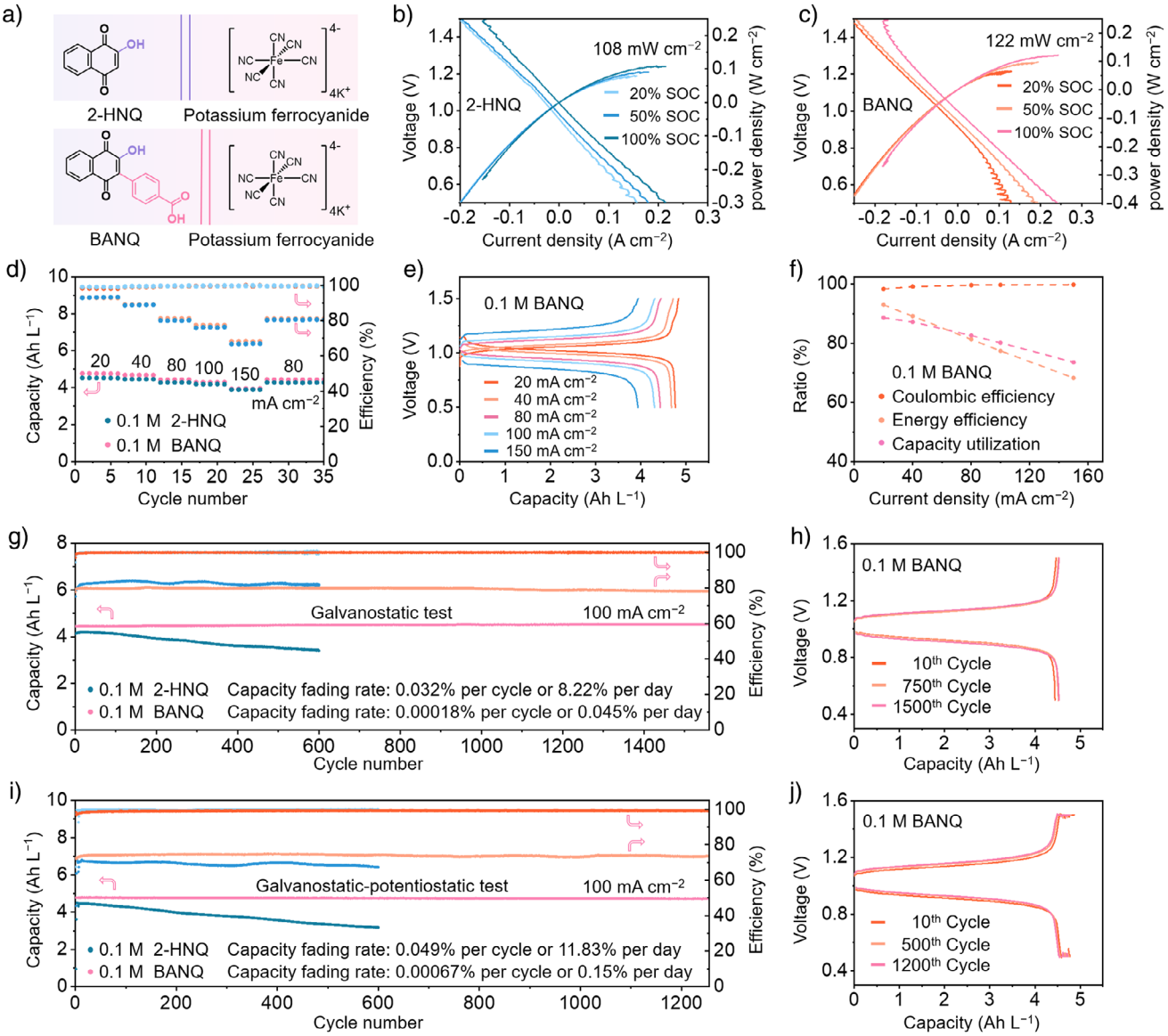

Figure 3. Electrochemical performances of 2-HNQ and BANQ. a) Molecular structures of 2-HNQ, BANQ and $K_4Fe(CN)_6$. b, c) Polarization and power density curves of (b) 0.1 M 2-HNQ||$K_4Fe(CN)_6$ and (c) 0.1 M BANQ||$K_4Fe(CN)_6$ AORFBs collected at different SOCs of 20%, 50%, and 100%. d) Coulombic efficiency, energy efficiency, and capacity retention of 0.1 M 2-HNQ||$K_4Fe(CN)_6$ and BANQ||$K_4Fe(CN)_6$ AORFBs at various current densities. e) Charge/discharge curves and f) Coulombic efficiency, energy efficiency, and capacity utilization of 0.1 M BANQ||$K_4Fe(CN)_6$ AORFBs at various current densities. g) Galvanostatic cycling performances of 0.1 M 2-HNQ||$K_4Fe(CN)_6$ and BANQ||$K_4Fe(CN)_6$ AORFBs with SPEEK membrane at a current density of 100 mA cm^{-2}. h) Charge/discharge profiles of 0.1 M BANQ||$K_4Fe(CN)_6$ AORFBs at 10^{th}, 750^{th}, and 1500^{th} cycles, respectively. i) Cycling performances of 0.1 M 2-HNQ||$K_4Fe(CN)_6$ and BANQ||$K_4Fe(CN)_6$ AORFBs upon galvanostatic-potentiostatic cycling. j) Charge/discharge profiles of 0.1 M BANQ||$K_4Fe(CN)_6$ AORFBs at 10^{th}, 500^{th}, and 1200^{th} cycles, respectively.

the non-planar asymmetric π-conjugated extension structure in enhancing the cycling stability. Additionally, CV tests of undiluted anolyte and catholyte after the entire cycling process (Figure S20) revealed no cross-over contamination of ferrocyanide in the anolyte or 2-HNQ/BANQ in the catholyte, indicating the effective suppression of transmembrane contamination by the custom-made SPEEK membrane. Meanwhile, CV analysis of the post-cycling 0.1 M 2-HNQ anolyte in the 0.1 M 2-HNQ||$K_4Fe(CN)_6$ AORFBs revealed the emergence of new irreversible peaks. This phenomenon suggests the potential occurrence of structural degradation in 2-HNQ during the cycling process. In contrast, no new peaks were detected in the CV spectra of the cycled 0.1 M BANQ anolyte. This observation further demonstrates that the non-planar asymmetric π-conjugated extended structure introduced by the benzoic acid substitution effectively maintains the molecular structural stability.

Given the promising prospects of BANQ for large-scale energy storage applications, we further investigated the electrochemical performance of 0.5 M BANQ||$K_4Fe(CN)_6$ AORFBs. Figure 4a depicts the open circuit voltages (OCVs) of 0.5 M BANQ||$K_4Fe(CN)_6$ AORFBs measured across

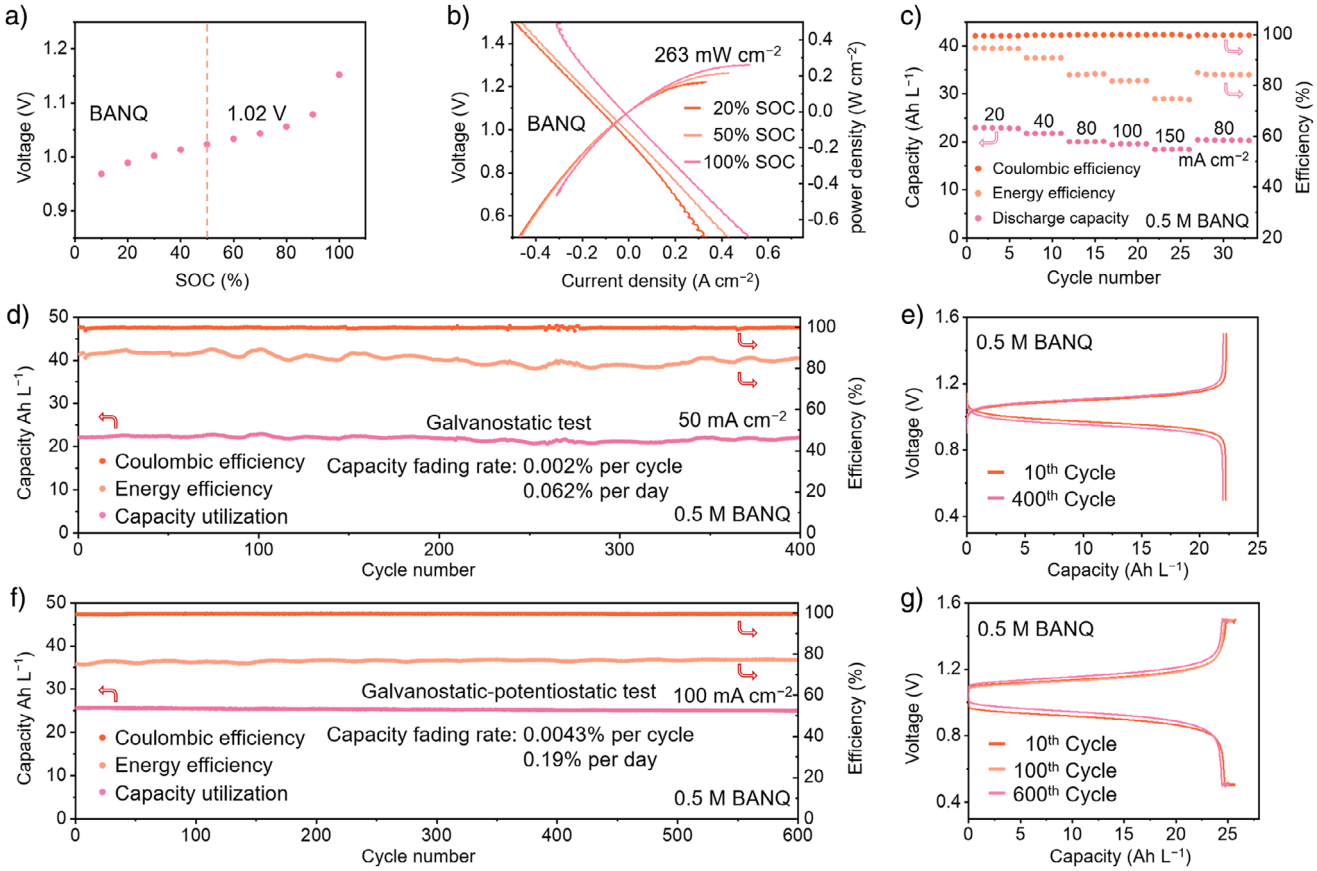

Figure 4. Cycling performances of 0.5 M BANQ||$K_4Fe(CN)_6$ AORFBs with SPEEK membrane. a) OCVs under different SOCs. b) Polarization and power density curves collected at SOCs of 20%, 50%, and 100%. c) Discharge capacity, Coulombic efficiency, and energy efficiency of 0.5 M BANQ||$K_4Fe(CN)_6$ AORFBs at galvanostatic current densities of 20, 40, 80, 100 and 150 mA cm^{-2}, respectively. d) Galvanostatic cycling performances of 0.5 M BANQ||$K_4Fe(CN)_6$ AORFBs with SPEEK membrane at a current density of 50 mA cm^{-2}. e) Charge/discharge profiles of 0.5 M BANQ||$K_4Fe(CN)_6$ AORFBs at 10^{th} and 400^{th} cycles, respectively. f) Cycling performances of 0.5 M BANQ||$K_4Fe(CN)_6$ AORFBs upon galvanostatic-potentiostatic cycling. g) Charge/discharge profiles of 0.5 M BANQ||$K_4Fe(CN)_6$ AORFBs at 10^{th}, 100^{th}, and 600^{th} cycles, respectively.

varying SOCs. The OCVs exhibit a linear rise from 10% to 90% SOC, attaining a value of 1.02 V at 50% SOC. Notably, the OCV exceeds 1.1 V at approximately 100% SOC, making it comparable to previously reported quinone-based AORFBs.[7] The polarization curves, recorded by LSV curves at 20%, 50%, and 100% SOCs are presented in Figure 4b. These curves reveal a notably high peak power density of 263 mW cm^{-2} at 100% SOC for the 0.5 M BANQ||$K_4Fe(CN)_6$ AORFBs, highlighting its superior power density relative to previously reported naphthoquinone derivatives.[17,18,22] Figure 4c and Figure S21 further illustrate the rate capability of the 0.5 M BANQ||$K_4Fe(CN)_6$ AORFBs. At current densities of 20 and 150 mA cm^{-2}, the Coulombic efficiencies remained nearly 100%, with corresponding discharge capacities of 22.9 and 18.5 Ah L^{-1}, and capacity utilizations of 85.4% and 69%, respectively. Notably, the SPEEK membrane displayed similar voltammetric characteristics at both 0.1 M and 0.5 M concentrations, suggesting that its performance remains unaffected by the concentration variation.

Moreover, we conducted extensive long-term cycling tests under both galvanostatic and galvanostatic-potentiostatic modes to examine the stability of 0.5 M BANQ||$K_4Fe(CN)_6$ AORFBs. As depicted in Figure 4d,e, under galvanostatic mode, the initial capacity of 0.5 M BANQ||$K_4Fe(CN)_6$ AORFBs was 22.2 Ah L^{-1}, which gradually declined to 22.0 Ah L^{-1} after 400 cycles (14.54 days), corresponding to a decay rate of 0.002% per cycle or 0.062% per day. Upon galvanostatic-potentiostatic cycling (Figure 4f,g), the initial capacity of 0.5 M BANQ||$K_4Fe(CN)_6$ AORFBs was 25.63 Ah L^{-1}, and the capacity remained approximately 24.97 Ah L^{-1} after running for 600 cycles (13.3 days), corresponding to a decay rate of merely 0.0043% per cycle (0.19% per day). These results demonstrated that the BANQ electrolyte exhibited excellent long-term cycling stability, with a capacity fade rate lower than previously reported naphthoquinone derivatives and comparable to those of state-of-the-art quinone-based AORFBs (Table S1).[16,17,22,34,40–53] This highlights the effectiveness of the asymmetric non-planar modification strategy in enhancing the stability of redox-active molecules.

To investigate the self-discharge characteristics of 0.5 M BANQ||$K_4Fe(CN)_6$ AORFBs, the battery was rested for 24 h at 100% SOC after being fully charged. Consequently, the OCV declined from 1.19 V to 1.11 V. Subsequently,

the discharge capacity exhibited a slight decline, reducing from 23.02 Ah L^{-1} to 21.98 Ah L^{-1}, corresponding to a low self-discharge ratio of 4.6% (Figure S22). Notably, the discharge capacity recovered to 22.81 Ah L^{-1} during the subsequent 4th cycle, demonstrating the high electrochemical stability of *re*-BANQ. The self-discharge behavior could be attributed to internal electron transfer across both electrolytes by the localized electron conduction through SPEEK membrane or the penetration of trace oxygen in ambient atmosphere, rather than decomposition of the BANQ anolyte electrolyte.

To further evaluate the electrochemical stability of BANQ anolyte at higher concentrations, we further tested a 1.0 M BANQ||$Na_4Fe(CN)_6$ AORFBs. The galvanostatic charge-discharge cycling results at 100 mA cm^{-2} show that the AORFBs delivered 82.5% of its theoretical capacity. After 210 cycles, the discharge capacity decreased slightly from 44.2 Ah L^{-1} to 44.0 Ah L^{-1}, corresponding to a capacity retention of 99.5% (Figure S23). The capacity fading rate is as low as 0.0045% per cycle, or 0.082% per day.

To elucidate the redox behavior and capacity decay mechanism of the BANQ||$K_4Fe(CN)_6$ AORFBs, a comprehensive suite of analytical techniques was applied to the BANQ anolyte, including in situ UV–vis absorption, in situ Fourier transform infrared (FTIR), ex situ electron paramagnetic resonance (EPR), and ex situ NMR spectroscopies (Figure 5a–e). First, in situ UV–vis absorption spectroscopy was employed to gain insights into the redox behavior of the naphthoquinone core in BANQ (Figure 5a). Upon discharging, BANQ anolyte presented a red color, and gradually transitioned to a yellow-brown upon being reduced. Upon charging, the absorption peak at λ_{446} nm gradually diminished, accompanied by the emergence of new absorption peaks at λ_{357} nm, along with shoulder peaks at λ_{431} nm and λ_{518} nm, indicating the transition from C═O to C─O─. The reversible shifts in absorption peaks demonstrated the good stability of the naphthoquinone redox core. Furthermore, in situ FTIR analysis was conducted to investigate the structural changes of BANQ during cycling (Figure 5b and Figure S24). Characteristic C═O stretching bands were observed at 1673 cm^{-1} (carbonyl groups) and 1654 cm^{-1} (carboxylic acid moieties). The 1673 cm^{-1} band, assigned to carbonyl groups, exhibited reversible intensity changes during redox processes. Concurrently, reduction-induced formation of C─O species was indicated by the appearance and progressive growth of a peak at 1344 cm^{-1}. A reversible O─H bending mode at 3122 cm^{-1} suggests the perturbation of aqueous O─H environments during reduction, consistent with enhanced hydrogen bonding interactions in the reduced state (Figure S25). Collectively, these reversible spectral features corroborate the high electrochemical reversibility of the BANQ molecule.

Ex-situ EPR analyses of the naphthoquinone redox core in BANQ were performed to investigate its electronic structure evolution during cycling (Figure 5c). The characteristic EPR resonance signal, centered at a magnetic field intensity of 3512.28 G (g-factor = 2.0048), was attributed to the formation of $BANQ^{3-\bullet}$ radical anion species. During charging, the EPR signal intensity gradually increased and broadened, with the maximum intensity observed at 50% SOC, after which the signal weakened and split at higher SOC values. This trend reflected a transient accumulation of $BANQ^{3-\bullet}$ radical anions, peaking at 50% SOC, followed by their gradual consumption during charging. This signal evolution was attributed to Heisenberg spin exchange, specifically the "flip-flop", dipolar-driven (zero-quantum) spin-exchange between two unpaired electrons when they come into close proximity, as well as intermolecular electron transfer.[54]

Ex-situ ^{1}H NMR spectroscopy was employed to further elucidate the impact of $BANQ^{3-\bullet}$ radical anions (Figure S26). During the charging process, initially, a noticeable high-field shift of the water peak was observed, reaching a maximum shift at 50% SOC. As the SOC increased over 50%, the water peak gradually shifted to lower fields, where the peak moved from 4.86 ppm to 4.84 ppm. This phenomenon indicates that the paramagnetic BANQ3$^{-\bullet}$ radical anions exhibit a strong shielding effect on water, resulting in an increased electron cloud density around the hydrogen nuclei in the aqueous phase and consequently causing a lower chemical shift of the resonance absorption peak.

To investigate the structural stability of BANQ molecule, its long-term chemical stability in 1.0 M KOH solution at high temperature and after long-term cycling was evaluated using ^{1}H NMR spectroscopy. After storing for 30 days at 50 °C, the ^{1}H NMR spectrum of BANQ solution remained unchanged (Figure S27). Even in the fully reduced state, no impurity signals were detected in the *re*-BANQ solution after prolonged storage (Figure S28). Besides, Figure 5d,e presents the ^{1}H NMR spectra of 2-HNQ and BANQ anolyte in their pre-charged state, as well as after undergoing galvanostatic or galvanostatic–potentiostatic cycling. After 600 galvanostatic cycles, the ^{1}H NMR spectrum of 2-HNQ anolyte revealed new impurity peaks emerging in both the aromatic and aliphatic regions. This is attributed to molecular degradation caused by enol-keto isomerization. In contrast, after over 500 galvanostatic cycles, the ^{1}H NMR spectrum of BANQ anolyte exhibited no additional impurity peaks, underscoring its good electrochemical stability. Notably, after extended galvanostatic-potentiostatic cycling, merely impurity signals were detected in the aromatic region. This finding suggests that exposure to elevated potential may promote the crossing of thermodynamic energy barriers by BANQ molecule, thereby initiating enol-keto isomerization and subsequent molecular degradation. Nonetheless, the relatively low intensity of the newly emerged NMR peaks indicated that the extent of degradation via isomerization still remained minimal.

DFT calculations were employed to further validate the above deduction and provide crucial theoretical insights into the chemical stability of BANQ and its possible isomers (Figure 5f). The calculation results indicate that the interconversion energy (ΔG) from 2-HNQ to molecule **1** is 35.54 kJ mol^{-1}, suggesting a high energy barrier for this transformation. Conversely, the interconversion energy from *re*-2-HNQ to molecule **2** was calculated to be –4.98 kJ mol^{-1}, indicating a lower energy barrier and implying that the isomerization of *re*-2-HNQ to molecule **2** in its reduced state is thermodynamically favorable. During this isomerization

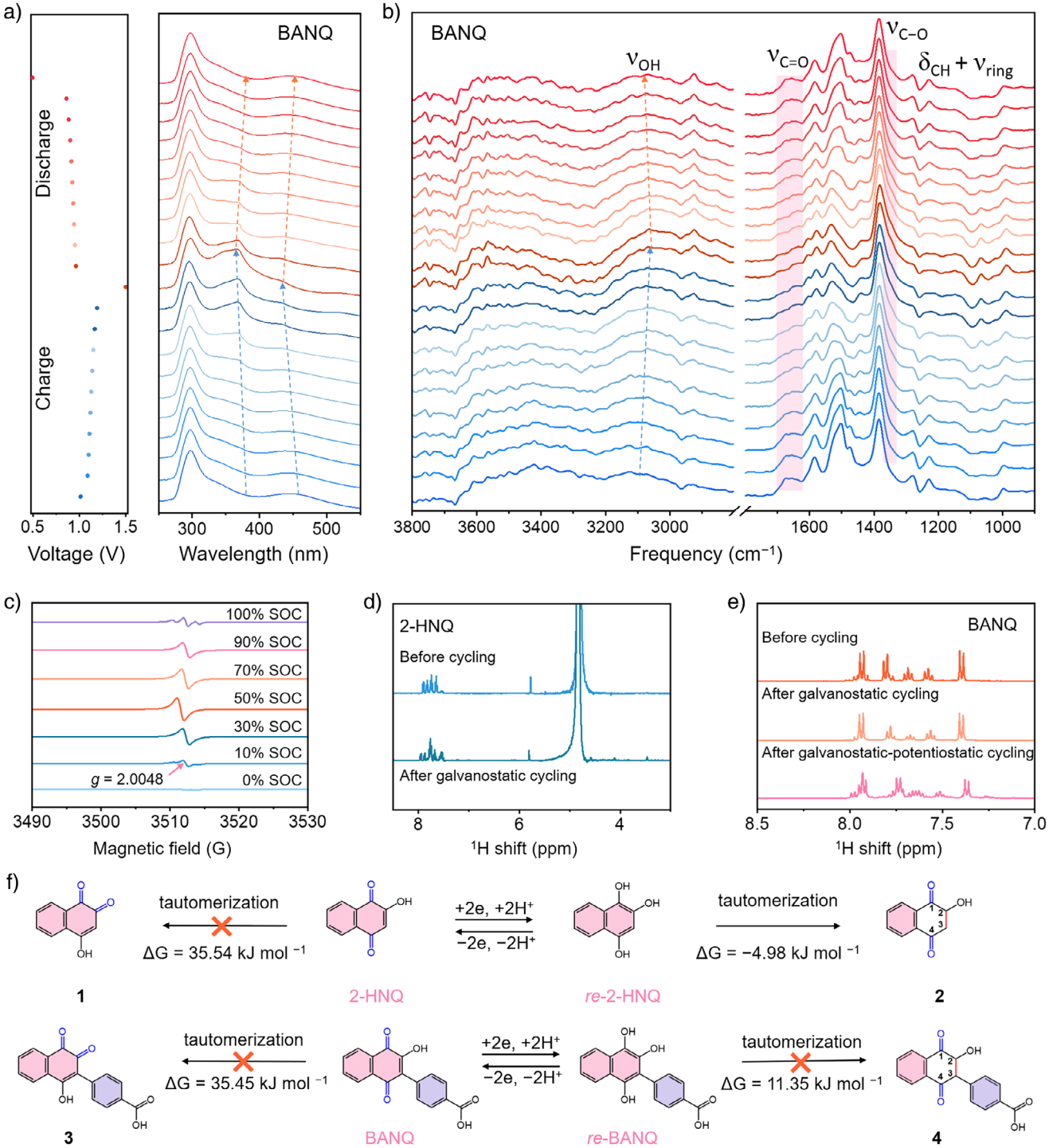

Figure 5. Redox and degradation mechanism studies of BANQ. a) In situ UV–vis absorption spectra and b) in situ FTIR spectra of BANQ anolyte during charge/discharge cycles. c) Ex situ EPR spectra of BANQ anolyte under different SOCs. d, e) ^{1}H NMR spectra of (d) 2-HNQ and (e) BANQ anolyte before cycling and after galvanostatic or galvanostatic-potentiostatic cycling. f) Proposed tautomerization pathways of 2-HNQ and BANQ, respectively.

process, the phenolic hydroxyl groups at C1 and C4 in *re*-2-HNQ undergo a structural transformation into C=O, while the double bond between C2 and C3 is reduced to a single bond. This structural transformation renders the quinone core of naphthoquinone incapable of undergoing reversible reduction to the phenolic hydroxyl form, thereby resulting in the loss of its redox reversibility and capacity. Similar interconversions have been reported in previous studies on various naphthoquinone derivatives, where the equilibrium and kinetics are strongly influenced by the substituents

attached to the naphthoquinone core.[17,18,22] In contrast, the tautomerization energy (ΔG) from BANQ to molecule **3** was determined to be 35.45 kJ mol^{-1}, which is comparable to that of 2-HNQ. However, the tautomerization energy from *re*-BANQ to molecule **4** was found to be 11.35 kJ mol^{-1}, suggesting that the isomerization of *re*-BANQ to molecule **4** in its reduced state is thermodynamically unfavorable. It verifies that the asymmetric non-planar π-conjugation modification of BANQ effectively alters the favorable thermodynamic trend of irreversible enol-keto tautomerization. Overall, these findings underscore the importance of rational molecular design in mitigating the spontaneous thermodynamic degradation of redox-active naphthoquinone derivatives.

Conclusion

In summary, here we report an asymmetric non-planar π-conjugation extension strategy to introduce polar benzoic acid groups into the active C─H positions of the naturally-occurring 2-HNQ molecule, achieving strongly enhanced aqueous solubility and electrochemical stability. The asymmetric, non-planar π-conjugation structure of BANQ, coupled with its pronounced deprotonation under alkaline conditions, induces a non-equilibrium charge distribution and increases molecular polarization, thereby significantly improving its water solubility in alkaline conditions. A detailed mechanistic analysis reveals that the non-planar, asymmetric π-conjugated modification effectively reduces the susceptibility of the redox core to electrophilic and nucleophilic attacks in alkaline aqueous solutions. Furthermore, in its reduced state, *re*-BANQ exhibits better thermodynamic stability than *re*-2-HNQ, rendering it less prone to enol-keto tautomerization and thereby preserving the structural integrity of the redox core. In result, the AORFBs based on 0.5 M BANQ anolyte achieves a capacity of 25.63 Ah L^{-1} and a high output power density of 264 mW cm^{-2}. It also maintains very low-capacity decay and self-discharge rates during long-term cycling, marking a notable improvement over natural naphthoquinone derivatives. This work underscores the significance of conjugated electron structure modification strategy for improving the comprehensive properties of organic redox-active molecules derived from natural sources, paving the way for the development of advanced AORFBs for sustainable, safe, and scalable energy storage.

Supporting Information

Essential experimental procedures/data can be found in the supplementary information.

Acknowledgements

This work was supported by the National Natural Science Foundation of China (U25A20628, 22561160129, 22479074, 22475096), the Equipment Pre-Research and Ministry of Education Joint Fund (8091B02052407), the Fundamental Research Program Key Project of Jiangsu Province (BK20253008), the Natural Science Foundation of Jiangsu Province (BK20240400, BK20241236), the Science and Technology Major Project of Jiangsu Province (BG2024013), the Scientific and Technological Achievements Transformation Special Fund of Jiangsu Province (BA2023037), the Academic Degree and Postgraduate Education Reforming Project of Jiangsu Province (JGKT24_C001), the Key Core Technology Open Competition Project of Suzhou City (SYG2024122), the Open Research Fund of Suzhou Laboratory (SZLAB-1308-2024-TS005), and the Chenzhou National Sustainable Development Agenda Innovation Demonstration Zone Provincial Special Project (2023sfq11).

Conflict of Interests

The authors declare no conflict of interest.

Data Availability Statement

The data that support the findings of this study are available in the Supporting Information of this article.

Keywords: Aqueous organic redox flow batteries · Energy storage · Keto-enol tautomerism · Natural naphthoquinone derivatives · Non-planar π-conjugated redox cores

[1] W. Wang, B. Yuan, Q. Sun, R. Wennersten. *J. Energy Storage* **2022**, *52*, 104812, https://doi.org/10.1016/j.est.2022.104812.
[2] Z. Zhu, T. Jiang, M. Ali, Y. Meng, Y. Jin, Y. Cui, W. Chen. *Chem. Rev.* **2022**, *122*, 16610–16751, https://doi.org/10.1021/acs.chemrev.2c00289.
[3] T. M. Gür. *Energy Environ. Sci.* **2018**, *11*, 2696–2767, https://doi.org/10.1039/c8ee01419a.
[4] A. A. Kebede, T. Kalogiannis, J. V. Mierlo, M. Berecibar. *Renewable Sustainable Energy Rev.* **2022**, *159*, 112213, https://doi.org/10.1016/j.rser.2022.112213.
[5] S. Koohi-Fayegh, M. A. Rosen. *J. Energy Storage* **2020**, *27*, 101047, https://doi.org/10.1016/j.est.2019.101047.
[6] J. Kim, Y. Kim, J. Yoo, G. Kwon, Y. Ko, K. Kang. *Nat. Rev. Mater.* **2022**, *8*, 54–70, https://doi.org/10.1038/s41578-022-00478-1.
[7] M. Pan, M. Shao, J. Zhong. *SmartMat* **2023**, *4*, e1198, https://doi.org/10.1002/smm2.1198.
[8] M. Sevket Guney, Y. Tepe. *Renewable Sustainable Energy Rev.* **2017**, *75*, 1187–1197, https://doi.org/10.1016/j.rser.2016.11.102.
[9] M. C. Argyrou, P. Christodoulides, S. A. Kalogirou. *Renewable Sustainable Energy Rev.* **2018**, *94*, 804–821, https://doi.org/10.1016/j.rser.2018.06.044.
[10] H. Zhang, W. Lu, X. Li. *Electrochem. Energy Rev.* **2019**, *2*, 492–506, https://doi.org/10.1007/s41918-019-00047-1.
[11] Z. Li, T. Jiang, M. Ali, C. Wu, W. Chen. *Energy Storage Mater.* **2022**, *50*, 105–138, https://doi.org/10.1016/j.ensm.2022.04.038.
[12] G. Yang, Y. Zhu, Z. Hao, Y. Lu, Q. Zhao, K. Zhang, J. Chen. *Adv. Mater.* **2023**, *35*, e2301898, https://doi.org/10.1002/adma.202301898.
[13] F. Hasan, V. Mahanta, A. A. A. Abdelazeez. *Adv. Mater. Interfaces* **2023**, *10*, 2300268, https://doi.org/10.1002/admi.202300268.
[14] J. Luo, B.o Hu, M. Hu, Y.u Zhao, T. L. Liu. *ACS Energy Lett.* **2019**, *4*, 2220–2240, https://doi.org/10.1021/acsenergylett.9b01332.

[15] J.-M. Fontmorin, S.è Guiheneuf, T. Godet-Bar, D. Floner, F. Geneste. *Curr. Opin. Colloid Interface Sci.* **2022**, *61*, 101624, https://doi.org/10.1016/j.cocis.2022.101624.
[16] C. Wang, Z. Yang, Y. Wang, P. Zhao, W. Yan, G. Zhu, L. Ma, B. Yu, L. Wang, G. Li, J. Liu, J. Zhong *ACS Energy Lett.* **2018**, *3*, 2404–2409, https://doi.org/10.1021/acsenergylett.8b01296.
[17] Y. Liu, P. Zhang, Z. Wu, G. Ding, X. Song, J. Ma, W. Wang, X.-Z. Wang, Z. Jin. *ACS Energy Lett.* **2024**, *9*, 586–593, https://doi.org/10.1021/acsenergylett.3c02530.
[18] W. Lee, G. Park, Y. Kwon. *Chem. Eng. J.* **2020**, *386*, 123985, https://doi.org/10.1016/j.cej.2019.123985.
[19] W. Lee, D. Park, G. Park, D. Chang, Y. Kwon. *Chem. Eng. J.* **2021**, *408*, 127320, https://doi.org/10.1016/j.cej.2020.127320.
[20] K. R. PriyaVallayil, S. Sankararaman. *Electrochim. Acta* **2022**, *407*, 139889, https://doi.org/10.1016/j.electacta.2022.139889.
[21] A. Shimizu, K. Takenaka, N. Handa, T. Nokami, T. Itoh, J.-I. Yoshida. *Adv. Mater.* **2017**, *29*, 1606592, https://doi.org/10.1002/adma.201606592.
[22] L. Tong, M.-A. Goulet, D. P. Tabor, E. F. Kerr, D. De Porcellinis, E. M. Fell, A. Aspuru-Guzik, R. G. Gordon, M. J. Aziz. *ACS Energy Lett.* **2019**, *4*, 1880–1887, https://doi.org/10.1021/acsenergylett.9b01321.
[23] K. Wedege, E. Dražević, D. Konya, A. Bentien, *Sci. Rep.* **2016**, *6*, 39101, https://doi.org/10.1038/srep39101.
[24] N. Miyaura, K. Yamada, A. Suzuki. *Tetrahedron Lett.* **1979**, *20*, 3437–3440, https://doi.org/10.1016/s0040-4039(01)95429-2.
[25] S. Borthakur, S. Baruah, B. Sarma, S. Gogoi. *Org. Lett.* **2019**, *21*, 2768–2771, https://doi.org/10.1021/acs.orglett.9b00726.
[26] G. Wurm, R. Probst, S. Schwandt. *Sci. Pharm.* **2001**, *69*, 257–264, https://doi.org/10.3797/scipharm.aut-01-196.
[27] X. Fernández-González, J. Miguel-Ávila, J.é Luis Mascareñas, M.ía Tomás-Gamasa. *ChenCatChem* **2025**, *17*, e202401778, https://doi.org/10.1002/cctc.202401778.
[28] A. K. Jordão, M. D. Vargas, A. C. Pinto, F. C. Silva, V. F. Ferreira. *RSC Adv.* **2015**, *5*, 67909–67943, https://doi.org/10.1039/c5ra12785h.
[29] W. S. Hamama, A. E.l-D. E. Hassanien, H. H. Zoorob. *J. Heterocycl. Chem.* **2017**, *54*, 2155-2196, https://doi.org/10.1002/jhet.2855.
[30] W. Yang, W. J. Mortier. *J. Am. Chem. Soc.* **1986**, *108*, 5708–5711, https://doi.org/10.1021/ja00279a008.
[31] R. Fu, T. Lu, F.-W. Chen. *Acta Phys.-Chim. Sin.* **2014**, *30*, 628–639, https://doi.org/10.3866/pku.Whxb201401211.
[32] Y. Deng, D. Yu, X. Cao, L. Liu, C. Rong, T. Lu, S. Liu. *Mol. Phys.* **2018**, *116*, 956–968, https://doi.org/10.1080/00268976.2017.1403657.
[33] B. Zhao, Y. Si, W. Guo, Y. Fu. *Adv. Funct. Mater.* **2022**, *32*, 2112225, https://doi.org/10.1002/adfm.202112225.
[34] C. Wang, B.o Yu, Y. Liu, H. Wang, Z. Zhang, C. Xie, X. Li, H. Zhang, J. Zhong *Energy Storage Mater.* **2021**, *36*, 417–426, https://doi.org/10.1016/j.ensm.2021.01.019.
[35] E. Runge, E. K. U. Gross. *Phys. Rev. Lett.* **1984**, *52*, 997–1000, https://doi.org/10.1103/PhysRevLett.52.997.
[36] K. Fukui, T. Yonezawa, C. Nagata, H. Shingu. *J. Chem. Phys.* **1954**, *22*, 1433–1442, https://doi.org/10.1063/1.1740412.
[37] K. Fukui, T. Yonezawa, H. Shingu. *J. Chem. Phys.* **1952**, *20*, 722–725, https://doi.org/10.1063/1.1700523.
[38] T. Lu, F. Chen. *J. Comput. Chem.* **2012**, *33*, 580–592, https://doi.org/10.1002/jcc.22885.
[39] H. Wang, S. Y. Sayed, E. J. Luber, B. C. Olsen, S. M. Shirurkar, S. Venkatakrishnan, U. M. Tefashe, A. K. Farquhar, E. S. Smotkin, R. L. McCreery, J. M. Buriak. *ACS Nano.* **2020**, *14*, 2575–2584, https://doi.org/10.1021/acsnano.0c01281.
[40] K. Lin, Q. Chen, M. R. Gerhardt, L. Tong, S. B. Kim, L. Eisenach, A. W. Valle, D. Hardee, R. G. Gordon, M. J. Aziz, M. P. Marshak. *Science* **2015**, *349*, 1529–1532.
[41] D. G. Kwabi, K. Lin, Y. Ji, E. F. Kerr, M.-A. Goulet, D. De Porcellinis, D. P. Tabor, D. A. Pollack, A.´n Aspuru-Guzik, R. G. Gordon, M. J. Aziz. *Joule* **2018**, *2*, 1894–1906, https://doi.org/10.1016/j.joule.2018.07.005.
[42] S. Jin, Y. Jing, D. G. Kwabi, Y. Ji, L. Tong, D. De Porcellinis, M.-A. Goulet, D. A. Pollack, R. G. Gordon, M. J. Aziz. *ACS Energy Lett.* **2019**, *4*, 1342–1348, https://doi.org/10.1021/acsenergylett.9b00739.
[43] S. Guiheneuf, T. Godet-Bar, J.-M. Fontmorin, C. Jourdin, D. Floner, F. Geneste. *J. Power Sources* **2022**, *539*, 231600, https://doi.org/10.1016/j.jpowsour.2022.231600.
[44] M. Wu, M. Bahari, E. M. Fell, R. G. Gordon, M. J. Aziz. *J. Mater. Chem. A.* **2021**, *9*, 26709-26716, https://doi.org/10.1039/d1ta08900e.
[45] C. Wang, Z. Yang, B.o Yu, H. Wang, K. Zhang, G. Li a, Z. Tie, J. Zhong *J. Power Sources* **2022**, *524*, 231001, https://doi.org/10.1016/j.jpowsour.2022.231001.
[46] M. Wu, Y. Jing, A. A. Wong, E. M. Fell, S. Jin, Z. Tang, R. G. Gordon, M. J. Aziz. *Chem* **2020**, *6*, 1432–1442, https://doi.org/10.1016/j.chempr.2020.03.021.
[47] Y. Jing, E. M. Fell, M. Wu, S. Jin, Y. Ji, D. A. Pollack, Z. Tang, D. Ding, M. Bahari, M.-A. Goulet, T. Tsukamoto, R. G. Gordon, M. J. Aziz. *ACS Energy Lett.* **2022**, *7*, 226–235, https://doi.org/10.1021/acsenergylett.1c02504.
[48] K. Amini, E. F. Kerr, T. Y. George, A. M. Alfaraidi, Y. Jing, T. Tsukamoto, R. G. Gordon, M. J. Aziz. *Adv. Funct. Mater.* **2023**, *33*, 2211338, https://doi.org/10.1002/adfm.202211338.
[49] Y. Ji, M.-A. Goulet, D. A. Pollack, D. G. Kwabi, S. Jin, D. D.e Porcellinis, E. F. Kerr, R. G. Gordon, M. J. Aziz. *Adv. Energy Mater.* **2019**, *9*, 1900039, https://doi.org/10.1002/aenm.201900039.
[50] Y. Liu, Z. Wu, P. Zhang, J. L.i JieWei, H. Wang, S. Wen, J. Liang, Y. Chen, T. Dai, Z. Tie, X. W. JingMa, Z. Jin. *Nat. Commun.* **2025**, *16*, 2965, https://doi.org/10.1038/s41467-025-58165-y.
[51] P. Zhang, J. W YuzhuLiu, ZuoaoWu, X. Song, G. Ding, J. L. HuaizhuWang, Z. Tie, Z. Jin. *Nat. Commun.* **2025**, *16*, 4727, https://doi.org/10.1038/s41467-025-59962-1.
[52] E. F. Kerr, Z. Tang, T. Y. George, S. Jin, E. M. Fell, K. Amini, Y. Jing, M. Wu, R. G. Gordon, M. J. Aziz. *ACS Energy Lett.* **2023**, *8*, 600–607, https://doi.org/10.1021/acsenergylett.2c01691.
[53] A. M. Alfaraidi, D. Xi, N. Ni, T. Y. George, T. Tsukamoto, R. G. Gordon, M. J. Aziz, R. Y. Liu. *ACS Appl. Energy Mater.* **2023**, *6*, 12259–12266, https://doi.org/10.1021/acsaem.3c01943.
[54] E. W. Zhao, E. Jónsson, R. B. Jethwa, D. Hey, D. Lyu, A. Brookfield, P. A. A. Klusener, D. Collison, C. P. Grey. *J. Am. Chem. Soc.* **2021**, *143*, 1885–1895, https://doi.org/10.1021/jacs.0c10650.

Manuscript received: September 09, 2025
Revised manuscript received: December 24, 2025
Manuscript accepted: January 05, 2026
Version of record online: January 12, 2026